

https://dspace.org/

Nucleation and growth of polar clusters with inphase tilts into a longrange ferroelectric matrix in a sodium niobate based complex relaxor

Harsh Kumar; Sanjit Ghose; Rudolph Erasmus; Saurabh Tripathi

AMER PHYSICAL SOC
https://hdl.handle.net/10539/45890
WOS

Downloaded from a DSpace repository. https://dspace.org/

Nucleation and growth of polar clusters with in-phase tilts into a long-range ferroelectric matrix in a sodium niobate based complex relaxor

Harsh Kumar [1], Sanjit Ghose [2], Rudolph Erasmus [3] and Saurabh Tripathi [1,*]

[1] *Department of Physics, Indian Institute of Technology (BHU), Varanasi 221005, India*

[2] *National Synchrotron Light Source II, Brookhaven National Laboratory, Upton, New York 11973, USA*

[3] *School of Physics and Microscopy and Microanalysis Unit, University of the Witwatersrand, WITS, Private Bag 3, Johannesburg 2050, South Africa*

(Received 23 December 2024; revised 26 May 2025; accepted 4 June 2025; published 23 June 2025)

In this study, we have investigated the temperature dependence of atomic ordering at multiple length scales in a lead-free sodium niobate-based relaxor, i.e., 0.75 $NaNbO_3$-0.25 $Ba_{0.9}Ca_{0.1}TiO_3$ (NN-25BCT) via synchrotron x-ray diffraction, Raman spectroscopy, and pair distribution function analysis. High-resolution synchrotron x-ray powder diffraction (SXRD) measurements reveal a ferroelectric phase transition in the relaxor ferroelectric NN-25BCT below the Vogel-Fulcher freezing temperature ($T_{VF} \approx 270$ K). In addition, SXRD analysis demonstrates the competition between in-phase octahedral tilting and ferroelectric order at the long-range scale using mode crystallography. On the other hand, Raman spectroscopic analysis provides evidence of polar ordering for $T > T_{VF}$ (with tetragonal symmetry) persisting up to the Burns temperature (T_B). Furthermore, pair distribution function (PDF) analysis reveals the presence of a polar antiferrodistortive tetragonal phase with *P4bm* space group at short ranges throughout the studied temperatures (i.e., 110 K $\leqslant T \leqslant$ 500 K), irrespective of nonpolar long-range ordering above T_{VF}. Therefore, our measurements provide direct evidence for the presence of polar ordering at short ranges and their gradual transformation into long-range polar ordering using an integrated multiscale structural analysis. As a result of a transition from relaxor to a ferroelectric phase in the vicinity of room temperature, NN-25BCT can be exploited for applications in pyroelectric detectors, electrocaloric devices, and multilayered ceramic capacitors.

DOI: 10.1103/szgf-l5rt

I. INTRODUCTION

Relaxor ferroelectrics (RFs) have consistently drawn attention of the scientific community due to their thermal stability and suitability for a wide range of applications, viz., multilayered ceramic capacitors, sensors, high-precision actuators, etc. [1–5]. Relaxor ferroelectrics are primarily characterized by two features: (i) diffuse dielectric permittivity (ϵ') around the maximum, and (ii) strong frequency dependence of temperature corresponding to dielectric maximum (T_m) [6–8]. Relaxor behavior in perovskite based (ABO_3) dielectric materials can be induced by substitution disorder at cationic sites, causing local random electric and/or elastic fields due to local charge imbalance and/or ionic radius mismatch, e.g., $Pb(Mg_{1/3}Nb_{2/3})O_3$, $Pb(Sc_{1/2}Ta_{1/2})O_3$, $Ba(Ti_{1-x}Zr_x)O_3$, $Ba(Ti_{1-x}Sn_x)O_3$, $(K_{1-x}Li_x)TaO_3$, etc. [4,5,9–14].

At high temperatures, relaxors remain in a nonpolar paraelectric phase, similar to the paraelectric phase of conventional ferroelectrics [5,15–18]. As the temperature decreases, they transform into an ergodic relaxor state [4]. In this state, nanoscale heterogeneities, known as polar nano regions (PNRs), nucleate and start to grow. These PNRs appear below the Burns temperature (T_B) and play a crucial role in tuning physical properties of relaxor ferroelectrics [4,19–21]. Immediately below T_B, there exists a short-lived correlation among PNRs, resulting in zero time-averaged polarization. Upon further cooling, an intermediate temperature T^* has been reported in relaxor ferroelectrics [22–24]. It is believed that below T^*, interaction among polar nano regions (PNRS) gradually enhances, and the system starts transforming into a static state from a dynamic state [19]. On further decreasing temperatures, relaxors eventually evolve into a glass-like structure below Vogel-Fulcher freezing temperature (T_{VF}) [19]. The state of relaxors below T_{VF} is referred to as nonergodic [25,26].

In contrast with conventional ferroelectrics, canonical relaxors do not exhibit a long-range ferroelectric phase below the temperature corresponding to the dielectric maximum [8]. However, a long-range ferroelectric ordering can be stabilized in canonical relaxors at low temperatures (below T_{VF}) on the application of an external electric field [27]. On the other hand, there are reports where long-range ferroelectric ordering can be stabilized solely by lowering the temperature below the Vogel-Fulcher freezing (T_{VF}) [16,28–31]. Based on the ordering below T_{VF}, relaxors can be classified into two categories. The first category include relaxors exhibiting a long-range ferroelectric order below T_{VF} [e.g., $PbMg_{1/3}Nb_{2/3}O_3$-x$PbTiO_3$ (PMN-PT)] [16] while the second category do not experience a ferroelectric phase transition even at the cryogenic temperatures [e.g., $PbMg_{1/3}Nb_{2/3}O_3$ (PMN)] [32,33]. To explain the above-mentioned relaxor to ferroelectric phase transition in

*Contact author: stripathi.phy@itbhu.ac.in

 ©2025 American Physical Society

relaxors, various models have been proposed [28,29]. Chu *et al.* used a description based on the bond strength of B-site cation to explain the ferroelectric phase transition in relaxors [28]. On the other hand, Dai *et al.* described the thermally driven relaxor to normal ferroelectric phase transition within a thermodynamic framework [29].

For decades, lead-based relaxor materials have been in vogue, but concerns over the toxic effects of lead on human health led researchers to explore lead-free alternatives that can provide similar properties [2]. In our earlier work, we reported a lead-free solid solution of $NaNbO_3$ (NN) and $Ba_{0.9}Ca_{0.1}TiO_3$ (BCT), where 0.75 $NaNbO_3$- 0.25 $(Ba_{0.9}Ca_{0.1})TiO_3$ (NN-25BCT) demonstrates relaxor behavior [13]. In the present work, we report the temperature evolution of short, medium, and long-range crystal structure of NN-25BCT in a temperature range 110 K $\leqslant T \leqslant$ 500 K . Dielectric analysis demonstrates nucleation and growth of polar nanoregions (PNRs) below the Burns temperature ($T \leqslant T_B$). Synchrotron x-ray diffraction (SXRD) data clearly reveal the relaxor to ferroelectric phase transition in NN-25BCT below T_{VF}. Distortion mode analysis of the low-temperature ferroelectric phase (SG: *P4bm*) provides experimental evidence of competitive interactions between long-range ferroelectric order and in-phase octahedral rotations. Raman spectroscopy, pair distribution function analysis, in conjunction with SXRD data refinements, suggest the presence of local polar order with tetragonal symmetry for $T > T_{VF}$ in the long-range paraelectric matrix.

II. EXPERIMENTAL

Samples with nominal composition 0.75 $NaNbO_3$-0.25 $Ba_{0.9}Ca_{0.1}TiO_3$ (NN-25BCT) were synthesized via the conventional solid-state reaction route. High-purity precursors including sodium carbonate (Na_2CO_3), barium carbonate ($BaCO_3$), calcium carbonate ($CaCO_3$), niobium pentoxide (Nb_2O_5), and titanium dioxide (TiO_2) were used as starting materials. Initially, the raw materials were weighed according to the desired stoichiometric ratios and subjected to ball milling for 24 hours in an ethanol medium. The resulting mixture was then calcined at 1000 °C for 5 hours under an air atmosphere. To eliminate any unreacted precursors or secondary phases, the calcined powders were ball-milled and recalcined under the same conditions. The final powders were compacted into cylindrical pellets using a uniaxial hydraulic press and subsequently sintered at 1100 °C for 4 hours. The synchrotron x-ray diffraction and PDF (pair distribution function) data were collected using beamline 28-ID-2 (x-ray powder diffraction, XPD) at NSLS2 (National Synchrotron Light Source), at Brookhaven National Laboratory, with a wavelength of 0.18210 Å. High-Q measurements were conducted with a maximum instrumental Q value (Q_{max}) of 25 Å^{-1}. Additionally, high-Q data for an empty borosilicate capillary were collected for background subtraction, which is necessary for converting the raw diffraction data into the total scattering structure function $S(Q)$. The $S(Q)$ was obtained from high-Q ($Q_{max} = 25$ Å^{-1}) SXRD data after performing standard normalization and background corrections on the raw scattering data using the PDFGETX3 program [34]. To obtain the corresponding reduced PDFs, the $S(Q)$ data were then Fourier-transformed using the function

$$G(r) = (2/\pi)\int_{Q_{min}}^{Q_{max}} Q[S(Q) - 1]\sin(Qr)dQ,$$

where $Q_{max} = 25$ Å^{-1} and $Q_{min} = 0.6291$ Å^{-1}. The structural refinements of the experimental atomic PDFs were carried out using the PDFGUI program [35].

Silver electrodes were fired on the top and bottom surfaces of the samples for the electrical measurements. The dielectric measurements were carried out using a Keysight LCR meter in the temperature range of 100–550 K. A precision LC II ferroelectric tester (Radiant Technologies Inc.) was used to obtain the polarization vs electric field (P-E) hysteresis loops and associated current vs electric field loops (*I-E*). Raman measurements were performed using a Horiba LabRAM HR spectrometer equipped with an Olympus BX41 microscope. An excitation wavelength of 514.5 nm from a Lexel Model-95 argon ion laser was used. Variable-temperature Raman spectra were collected by placing the samples in a Linkam THMS600 temperature-controlled microscope stage. The laser beam was focused onto the sample surface using a 50× LWD objective lens (numerical aperture = 0.50), and the backscattered signal was dispersed using a 600 lines/mm grating and detected with a liquid nitrogen-cooled CCD. Data acquisition was carried out using LabSpec v5 software. The laser power at the sample surface was maintained at approximately 0.4 mW, and care was taken to ensure the absence of any laser-induced local heating effects. All Raman spectra were corrected using the Bose-Einstein temperature factor as follows:

$$I_c(\tilde{\nu}) = \frac{I_m(\tilde{\nu})}{n(\tilde{\nu}, T) + 1} \quad \text{where} \quad n(\tilde{\nu}, T) = \frac{1}{\exp\left(\frac{hc\tilde{\nu}}{kT}\right) - 1}.$$

Here, $I_c(\tilde{\nu})$ is the corrected Raman intensity, $I_m(\tilde{\nu})$ is the measured intensity, and $n(\tilde{\nu}, T)$ is the Bose-Einstein thermal population factor, with $\tilde{\nu}$ representing the wave number. Furthermore, Raman spectra were deconvoluted and fitted using the Lorentzian function.

III. RESULTS AND DISCUSSION

A. Long-range structural analysis

In our previous paper, we examined composition-dependent phase transitions of $(1-x)$ $(NaNbO_3) - x$ $Ba_{0.9}Ca_{0.1}TiO_3$ (NN-xBCT) for $0.00 \leqslant x \leqslant 1.00$ [13]. We observed a relaxor ferroelectric-like behavior for $x = 0.25$, characterized by a high diffusion coefficient ($\gamma = 1.94$). Figure 1(a) illustrates temperature-dependent real (ϵ') and imaginary (ϵ'') parts of dielectric permittivity at various frequencies (1 kHz to 1 MHz) in the temperature range 100 K $\leqslant T \leqslant$ 550 K. The real part of dielectric permittivity exhibits a diffuse nature around the maximum ($T_m \approx 285$ K) and demonstrates a typical relaxor behavior. This relaxor behavior can be attributed to the presence of multiple cations with different oxidation states and/or sizes occupying the same crystallographic site, resulting in local strain and local fields simultaneously. Figure 1(c) shows the inverse of dielectric permittivity ($1/\epsilon'$) as a function of temperature at 10 kHz. For NN-25BCT, the dielectric permittivity deviates from the Curie-Weiss law above T_m (≈285 K). However, $1/\epsilon'$ exhibits

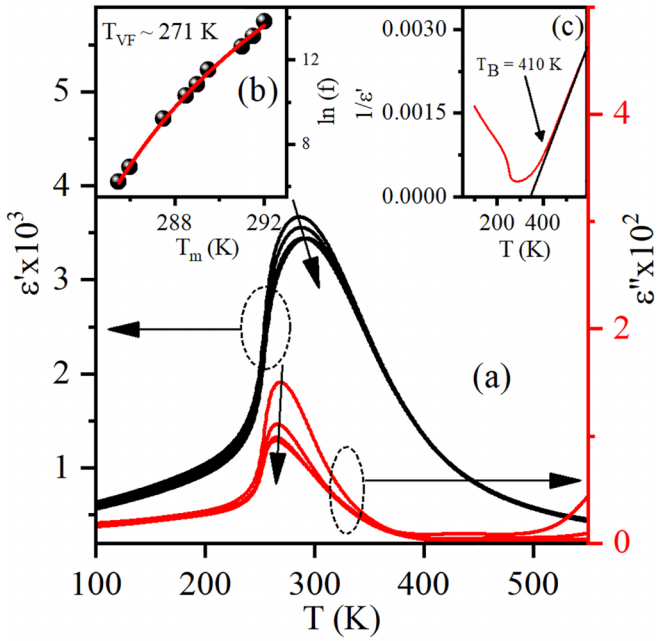


FIG. 1. (a) Temperature-dependent evolution of real and imaginary part of dielectric permittivity. (b) Vogel-Flucher fitting of the temperatures corresponding to the dielectric to estimate the freezing temperature. (c) The inverse of dielectric permittivity as a function of temperature, marking the Burns temperature.

linear behavior above $T \approx 410$ K. The temperature at which the deviation occurs is referred to as the Burns temperature T_B. This temperature T_B marks the onset of nucleation and growth of polar nanoregions (PNRs) that become more pronounced as the temperature decreases. At high temperatures (but below T_B), these PNRs are mobile, and their dynamics slow down on cooling. The PNRs freeze in a glass-like state below a temperature ($T = T_{VF}$), which can be determined using the Vogel-Fulcher (V-F) relation:

$$f = f_0 \exp\left[-\frac{E_a}{k(T_{\max} - T_{VF})}\right], \tag{1}$$

where T_{VF} is the static freezing temperature, E_a is the activation energy, f_0 is an attempt frequency, and T_{max} is the temperature of the dielectric permittivity maximum [36,37]. Figure 1(b) shows Vogel-Fulcher fitting of the real part of the permittivity of NN-25BCT in the frequency range of 500 Hz to 1 MHz. The data were well-fitted by the Vogel-Fulcher equation with a pre-exponential factor $f_0 = 7.68\times10^{12}$ Hz, activation energy $E_a = 0.028$ eV, and Vogel-Fulcher freezing temperature $T_{VF} \approx 271$ K, respectively. These values closely align with those reported on similar materials [2,38]. Moreover, it has been reported earlier that relaxors with activation energy close to the present value transform into a long-range ferroelectric phase at low temperatures [28]. Therefore, we aim to explore the relaxor-to-ferroelectric phase transition below freezing temperature T_{VF} (if any).

To explore temperature-dependent structural phase transitions of NN-25BCT, we have performed synchrotron x-ray diffraction measurements. The indexing of the diffraction pattern has been done with respect to a doubled perovskite cell (dpc). Figures 2(b)–2(d) depicts main perovskite reflections, viz., $\{400\}_{dpc}$, $\{440\}_{dpc}$, and $\{444\}_{dpc}$ for a temperature range 110 K $\leqslant T \leqslant$ 500 K. Figure 2(a) demonstrates the appearance of the superlattice reflection(s) upon decreasing temperature below 400 K. At 500 K, all the reflections are singlet in nature: a typical feature of high-temperature phase in relaxors having a cubic structure with $Pm\bar{3}m$ space group [29,39]. At low temperatures, a weak shoulder appears near $\{400\}_{dpc}$ at a lower 2θ and $\{440\}_{dpc}$ becomes asymmetric. Moreover, we see the appearance of a weak superlattice reflection near $\{222\}_{dpc}$ reflection for $T \leqslant 400$. This weak reflection was indexed as $\{310\}$ with respect to the doubled perovskite cell and is associated with in-phase octahedral rotation [40]. The superlattice reflection remains stable down to the lowest studied temperature, i.e., 110 K. The main perovskite reflections, viz., $\{h00\}_{dpc}$ and $\{hh0\}_{dpc}$ split into two peaks, whereas $\{hhh\}_{dpc}$ reflections remain singlet, suggesting a tetragonal symmetry. Such splitting of main perovskite reflections has been observed in pure $NaNbO_3$ at high temperatures [SG: $P4/mbm$ (paraelectric); tilt system: $a^0a^0c^+$ in Glazer's notation [41,42]] and $BaTiO_3$ at ambient conditions [SG: $P4mm$ (ferroelectric)] [43]. However, the presence of superlattice reflections along with splitting in the main perovskite reflections of NN-25BCT discards the barium titanate-like tetragonal phase (SG: $P4mm$), which results only due to octahedral distortion. Following the literature on similar systems, a plausible ferroelectric tetragonal phase with in-phase octahedral rotations is $P4bm$ space group (tilt system: $a^0a^0c^+$ in Glazer's notation [41,42], cell size: $\sqrt{2}a_p\times\sqrt{2}a_p\times c_p$) which can be visualized as a "polar version" of the tilt orientated tetragonal phase observed in the paraelectric region of $NaNbO_3$ [40,43,44]. The presence of a superlattice reflection (due to an in-phase octahedral tilt) and splitting of the main perovskite reflections suggests a paraelectric tetragonal phase with a $P4/mbm$ (T1) space group at ambient conditions. Nonetheless, a ferroelectric tetragonal model [SG: $P4bm$ (T2)] is plausible below the V-F freezing temperature, i.e., $T_{VF} \approx 270$ K. To confirm the evolution of the crystallographic structures as a function of temperature, Rietveld refinements of the diffraction patterns have been carried out using the FULLPROF package [45]. We have used the following models to fix the diffraction patterns: (i) $Pm\bar{3}m$ (PE) [410 K $\leqslant T \leqslant$ 500 K], (ii) $P4/mbm$ (PE) [270 K $\leqslant T \leqslant$ 400 K], (iii) $P4bm$ (FE) [110 K $\leqslant T \leqslant$ 260 K]. The choice of these models has been made on the basis of splitting in main perovskite reflections, the appearance of superlattice reflections, and following the literature on similar materials [40,44,46]. Figure S1 in the Supplemental Material file depicts the fitted diffraction patterns of NN-25BCT for some representative temperatures (see Ref. [47]). Tables S1–S3 of the Supplemental Material present the lattice parameters, atomic coordinates, thermal parameters, and goodness of fit parameter (R_{wp}) obtained after refinements of the diffraction patterns collected at various temperatures (see Ref. [47]). Figure 2(e) shows the evolution of reduced lattice parameters as a function of temperature. The transition from a centrosymmetric tetragonal phase with $P4/mbm$ space group (paraelectric) to a noncentrosymmetric tetragonal phase with $P4bm$ space group (ferroelectric) is evident from a discontinuity in the unit-cell volume and a nonanalytical behavior

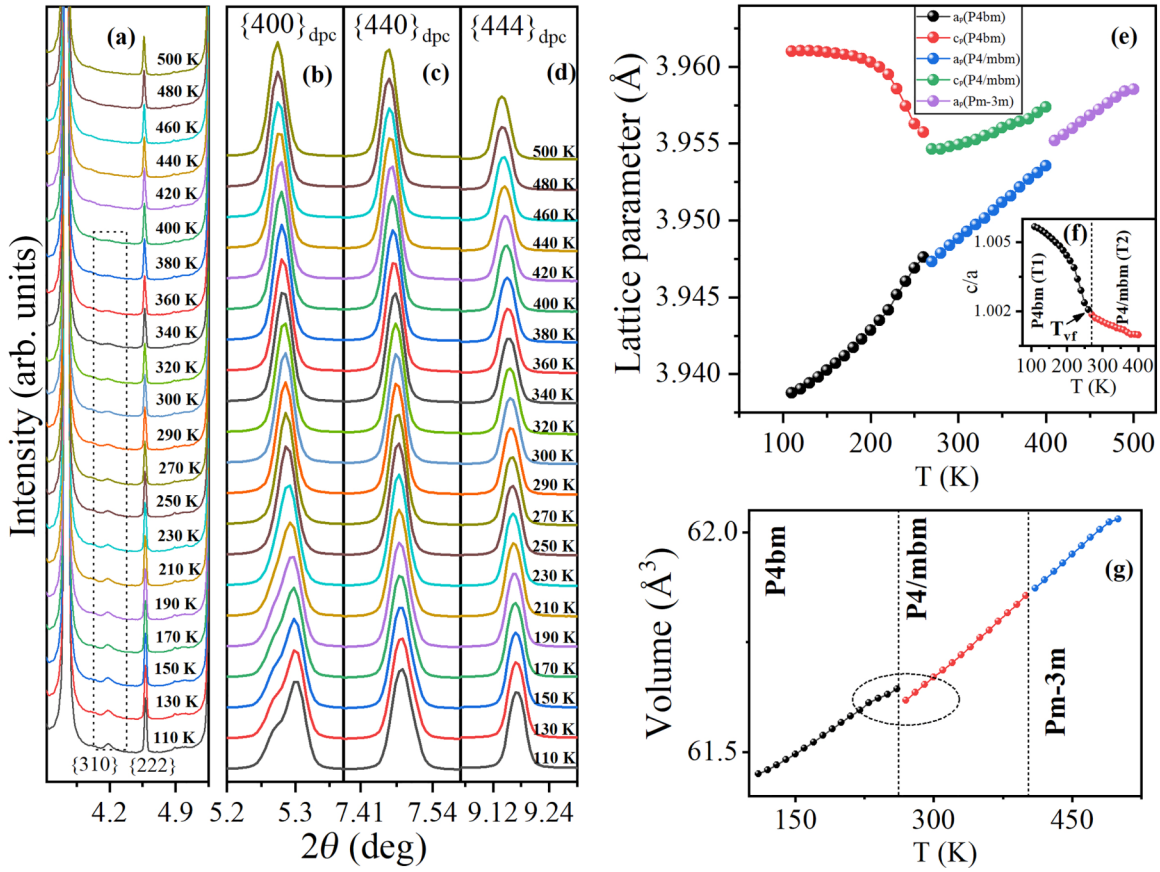


FIG. 2. Temperature-dependent evolution of some representative (a) superlattice reflections, (b)–(d) main perovskite reflections. Evolution of (e) lattice parameters, (f) tetragonality, and (g) volume of the elementary cell as a function of temperature.

in tetragonality around $T \approx 270$ K. This temperature coincides with the V-F freezing temperature $T_{VF} \approx 270$ K [see Figs. 2(f) and 2(g)]. Similar characteristics of the phase transitions are also observed for PMN-PT, PZN, etc., where relaxors undergo a long-range ferroelectric phase transition below Vogel-Fulcher freezing temperature (T_{VF}) [16,28–31]. Henceforth, Rietveld refinements, along with reasonable agreement factors, suggest a long-range ferroelectric order below the V-F freezing temperature T_{VF} in the present system exhibiting relaxor-like characteristics. Similar to lead-based relaxors, displaying an average cubic structure with rhombohedral clusters at short ranges (that transform into a long-range rhombohedral phase below the freezing temperature T_{VF}), NN-25BCT exhibits an average centrosymmetric antiferrodistortive tetragonal structure (SG: $P4/mbm$) at room temperature with polar clusters. These polar clusters transform into a noncentrosymmetric tetragonal ferroelectric phase (SG: $P4bm$) upon cooling.

The structure of an ideal perovskite is cubic with $Pm\bar{3}m$ space group [6]. However, most of the perovskites exhibiting fascinating properties are distorted. There exist three different types of distortions: (i) distortion of BO_6 octahedra, (ii) cationic displacements (parallel or antiparallel), and (iii) tilting of BO_6 octahedra with respect to each other [41,42]. It is important to note that these distortions can occur independently or in combination with each other. Correlated identical displacements of B-site cations are responsible for ferroelectricity and are linked with the Γ ($k = 0, 0, 0$) point of the cubic Brillouin zone. On the other hand, in-phase and out-of-phase octahedral tilting result in cell multiplication and are linked with M ($k = 1/2, 1/2, 0$) and R ($k = 1/2, 1/2, 1/2$) points of cubic Brillouin zone [41,42]. The distortions present in the low-symmetry structures correspond to a mode or modes that are soft in the high-symmetry cubic structure [48,49]. Furthermore, these soft modes are associated with the irreducible representations of the parent space group [48,49]. Symmetry-mode analysis quantifies the contribution of different modes in the low-symmetry distorted structure. In the present work, the low-temperature phase of NN-25BCT is ferroelectric, having a tetragonal symmetry with the $P4bm$ space group (tilt system: $a^0a^0c^+$). For quantifying the structural distortions, we used the AMPLIMODES program available at the Bilbao Crystallographic server [48,49]. As input for AMPLIMODES, we have used the high-symmetry cubic phase (SG: $Pm\bar{3}m$ and $a_0 = 3.95854$ Å) as a reference (parent) structure and the low-symmetry tetragonal (SG: $P4bm$) phase as a distorted structure. To describe the atomic positions of the undistorted cubic phase, we used a Wyckoff sequence in which A, B, and O atoms occupy 1b (1/2, 1/2, 1/2), 1a (0,0,0), and 3d (1/2, 0, 0) sites, respectively. The transition from the cubic phase to the tetragonal phase occurs through the splitting of the Wyckoff sites (see Table I).

As indicated in Table I, the two modes, Γ_4^- and M_3^+, are responsible for the symmetry-breaking transition $Pm\bar{3}m \rightarrow P4bm$. These irreducible representations (irrep), viz. M_3^+ and Γ_4^- are linked with the zone boundary and the zone center

TABLE I. Wyckoff site splitting in high- and low-symmetry structures with corresponding symmetry-breaking modes. Here, A and B represent the atoms positioned at the A and B sites of the perovskite structure.

	Wyckoff site splitting	
SG: $Pm\bar{3}m$	Symmetry-breaking modes	SG: $P4bm$
A 1*b*	Γ_4^-	A 2*b*
B 1*a*	Γ_4^-	B 2*a*
O 3*d*	Γ_4^-, M_3^+	O1 2*a*, O2 4*c*

of the cubic Brillouin zone, leading to in-phase rotations of adjacent octahedra and ferroelectric displacements in the unit cell, respectively. Therefore, we can quantify in-phase octahedral rotations and ferroelectric displacements by calculating the amplitudes of M_3^+ and Γ_4^- modes using AMPLIMODES. Now, the effect of octahedral rotations on ferroelectricity in the perovskite-based systems has been a matter of discussion for the last several decades [50–53]. Generally, ferroelectricity (polar displacements) in perovskite-based systems increases with a decrease in temperature, and hence, the amplitude of the Γ_4^- phonon mode would increase with decreasing temperatures [54]. Figure 3 illustrates the temperature-dependent evolution of the amplitude of Γ_4^- and M_3^+ modes. From 260 to 220 K, the amplitude of M_3^+ mode increases and reaches its saturation value below 200 K. On the other hand, the amplitude of the Γ_4^- mode initially decreases up to 200 K, after which it increases with decreasing temperature. It is important to note that the amplitude of the Γ_4^- mode starts showing its obvious effect (i.e., increase in amplitude with the decrease in temperature) once the amplitude of M_3^+ mode reaches saturation. It is widely reported in the literature that octahedral tilts have detrimental effects on ferroelectricity for B-site-driven ferroelectric materials [52,53,55–57], which can be observed as a reduction in the amplitude of the Γ_4^- mode. Thus, our experimental science results provide evidence for the competitive nature of octahedral tilts with ferroelectric displacements.

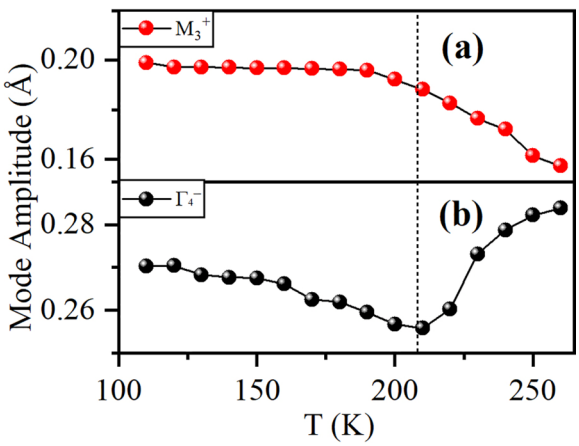


FIG. 3. Temperature-dependent evolution of (a) M_3^+ and (b) Γ_4^- modes in the stability region of long-range ferroelectric phase with *P*4*bm* space group calculated using the information obtained from refinement of SXRD patterns.

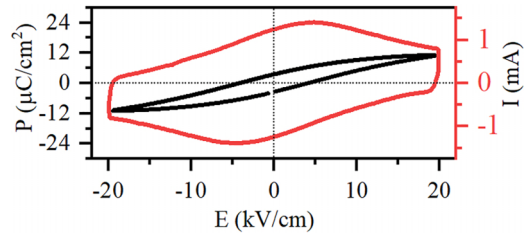


FIG. 4. Room-temperature polarization vs electric field (P-E) and associated current vs electric field (*I*-*E*) loops of NN-25BCT measured at a maximum electric field of 20 kV/cm. The slim hysteresis loop is characteristic of a relaxor-like behavior.

B. Short-range structural analysis

Figure 4 shows polarization vs electric field (*P*-*E*) and current vs electric field (*I*-*E*) loops at a maximum field of

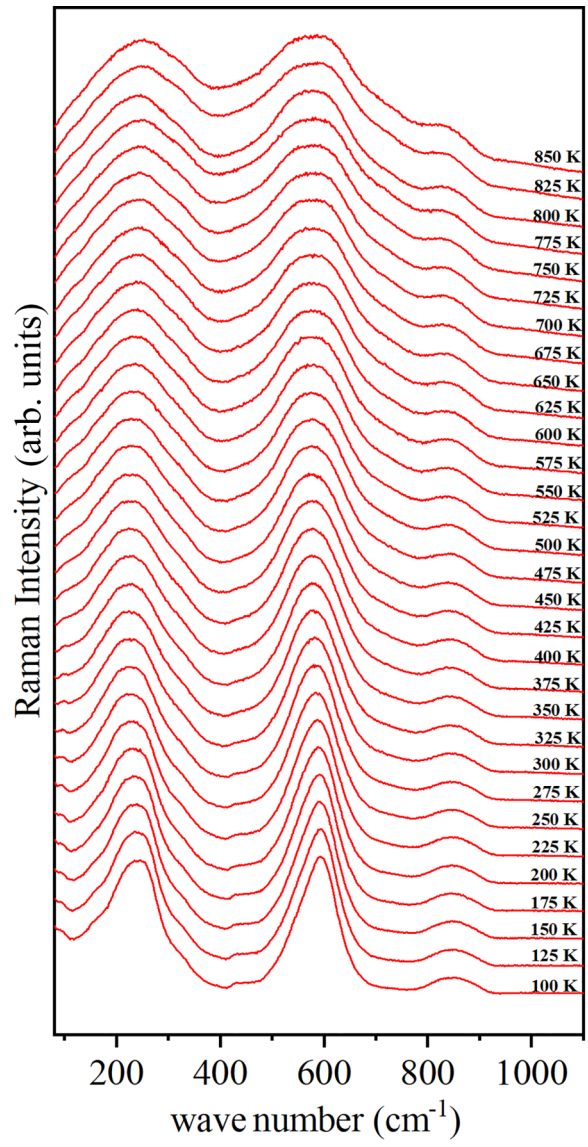


FIG. 5. Variable-temperature Raman spectra of NN-25BCT in the temperature range $100\,\text{K} \leqslant T \leqslant 850$ K. The Raman spectra shown here have been taken during the heating cycle using the protocol described in the experimental section.

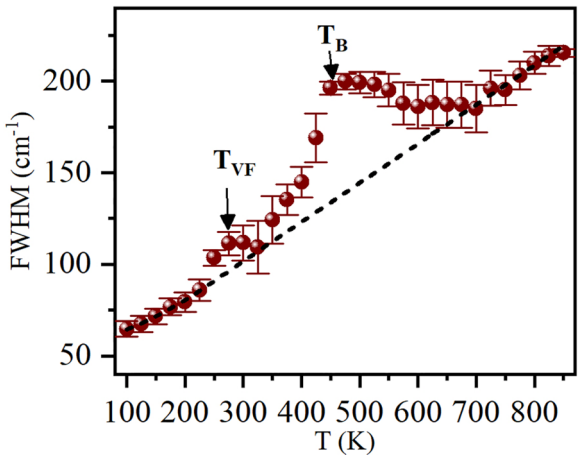


FIG. 6. Temperature-dependent variation of the FWHM of the Raman mode located near 250 cm^{-1}. The black dashed line is a polynomial baseline to account for the trivial increase in phonon widths on heating.

20 kV/cm and in ambient conditions. It is important to note that the slim hysteresis (*P-E*) loop and the switching peaks in the *I-E* curve suggest ferroelectric characteristics contrary to the long-range centrosymmetric structure with a tetragonal symmetry (SG: $P4/mbm$) at room temperature (i.e., 300 K). This ferroelectric response likely stems from the correlation among short-range ordered polar nanoregions typical of relaxors. To explore short-range ordering and their symmetry, temperature-dependent Raman spectroscopy has been employed [13,58–60]. We have collected the temperature-dependent Raman spectra in the temperature range 100 K $\leqslant T \leqslant$ 850 K in the heating and cooling cycles (see Fig. 5; for clarity, only the heating-cycle data are shown). It was observed that the spectral changes are fully reversible, without a temperature hysteresis within the experimental accuracy. All the Raman spectra were corrected for the Bose-Einstein population factor [61]. The Raman spectra can be decomposed into two distinct types of vibrational modes: (i) motion of A-site cation with respect to BO_6 octahedra (external modes) and (ii) isolated vibration of BO_6 octahedra involving bending and stretching modes (internal modes) [62]. At the lowest temperature (i.e., $T = 100$ K), there are three prominent broad peaks present around 250, 600, and 850 cm^{-1}. The Raman scattering near 250 cm^{-1} in the spectra of perovskite-type ferroelectric solid solutions is dominated by vibrations of off-centered B-site cations [63]. The Raman band near 600 cm^{-1} arises from BO_6 stretching modes, whereas the weak band near 800 cm^{-1} stems from a combination mode [62,64,65]. Significant Raman scattering was detected above the Burns temperature T_B, where the long-range structure is $Pm\bar{3}m$, with all atoms positioned at sites possessing a center of inversion. As we know, first-order Raman scattering is prohibited for a centrosymmetric structure, so such scattering is often attributed to cationic disorder or second-order effects [60,62]. From the SXRD and dielectric analyses, it becomes evident that in NN-25BCT, a long-range polar phase exists only below the V-F freezing temperature T_{VF} (≈270 K). Therefore, signatures of Raman modes at high temperatures offer strong evidence for the presence of ferroelectric ordering at short ranges (PNRs). Similar Raman spectra have also been reported earlier in related systems, where the ferroelectric ordering with tetragonal symmetry has been observed at short ranges [40,66]. All the Raman spectra were fitted using a suitable number of Lorentz peaks (see Fig. S2 in the Supplemental Material [47]). To shed light on the coupling processes between the B-site local dipoles, we plotted the full width at half maximum (FWHM) of the Raman scattering near 250 cm^{-1} against temperature

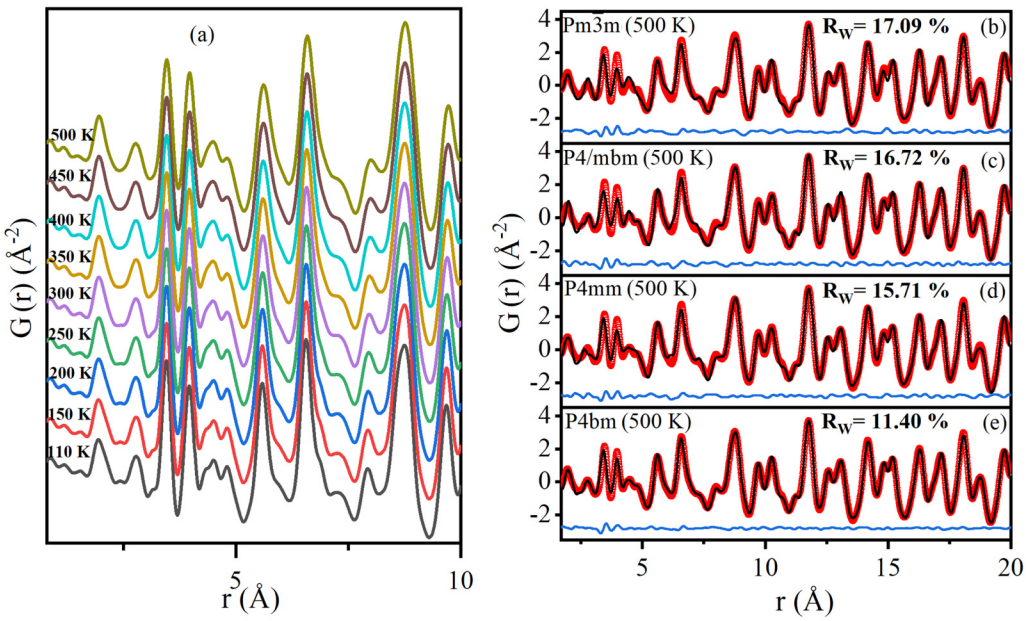


FIG. 7. (a) Temperature dependent evolution of PDF profiles of NN-25BCT. Atomic PDF fitting at 500 K using different plausible models viz., (b) Pm-3m (c) P4/mbm, (d) P4mm, (e) P4bm. The goodness of fit parameter suggests that the P4bm model produces the best fit to the data.

(Fig. 6). It is clear that between 200 and 700 K, the data points deviate from the trivial gradual increase of the phonon width with temperature (see the dashed line in Fig. 6), indicating ongoing local-scale rearrangements in the subsystem of off-centered B-site cations in the entire temperature range 200–700 K. The two maxima, near 270 and 420 K, mark the characteristic temperatures of structural transformations due to coupling of the B-site dipoles, which match very well T_{VF} and T_B derived from the temperature dependence of the dielectric permittivity (Fig. 1).

Generally, it has been observed in relaxors that the symmetry at long ranges is higher than the symmetry at short ranges (PNRs) [43,67–71]. Pair distribution function (PDF) analysis is widely used for quantitative analysis of short-range structural distortions [72,73]. Understanding such short-range structural distortions can provide insight into the relaxor-to-ferroelectric transition in NN-25BCT. In many relaxor systems, it has been observed that the long-range symmetry at low temperatures matches the short-range symmetry (PNRs) at the high-temperature nonpolar phase [28,29,32,39]. Figure 7(a) shows the temperature-dependent atomic PDF profiles of NN-25BCT in a temperature range of $110\ \text{K} \leqslant T \leqslant 500$ K. We do not see any significant changes in atomic PDF profiles upon increasing the temperature, except peak broadening, which is indicative of increased thermal disorder at high temperatures. We used the following plausible models to fit the experimental $G(r)$ at 500 K:

(i) $Pm\bar{3}\,m$ (cubic): corresponding to long-range symmetry at $T > 400$ K confirmed after Rietveld refinements.

(ii) $P4/mbm$ (tetragonal): corresponding to long-range symmetry of ergodic phase stable for $270\ \text{K} \leqslant T \leqslant 400$ K.

(iii) $P4bm$ (tetragonal): corresponding to long-range symmetry stable for $110\ \text{K} \leqslant T \leqslant 260$ K.

(iv) $P4mm$ (tetragonal): corresponding to long-range symmetry of $B_{0.9}Ca_{0.1}TiO_3$ (BCT) at room temperature [74,75].

These models were inferred from the analysis of synchrotron x-ray diffraction data in conjunction with the literature [40,66,76]. Figures 7(b)–7(e) depict PDF fits of different models with goodness of fit parameter R_w. We see that the tetragonal $P4bm$ model provides the best fit with the lowest value of R_w. Therefore, we can conclude that the short-range structure at 500 K is polar with tetragonal symmetry (space group: $P4bm$) similar to what has been observed in barium titanate where long-range rhombohedral (polar) symmetry of low temperatures is stable at short ranges in the high-temperature paraelectric phase with cubic symmetry (space group: $Pm\bar{3}m$) [77]. Furthermore, the lowest R_w was achieved with the $P4bm$ model for all the PDF patterns (i.e., at all temperatures). Moreover, we see that the tetragonal phase at short ranges (space group: $P4bm$) is the same as the low-temperature phase of NN-25BCT stable at long ranges (concluded from SRXD analysis). Figure 8 depicts the temperature-dependent fittings of experimental $G(r)$ at some representative temperatures within the spatial range $1.7\ \text{Å} \leqslant r \leqslant 20$ Å. To quantify the ferroelectric content at short ranges, symmetry-mode analysis was performed using atomic coordinates and lattice parameters obtained from the PDF refinements. As discussed earlier, the ferroelectric content of the short-range ordered (SRO) tetragonal phase

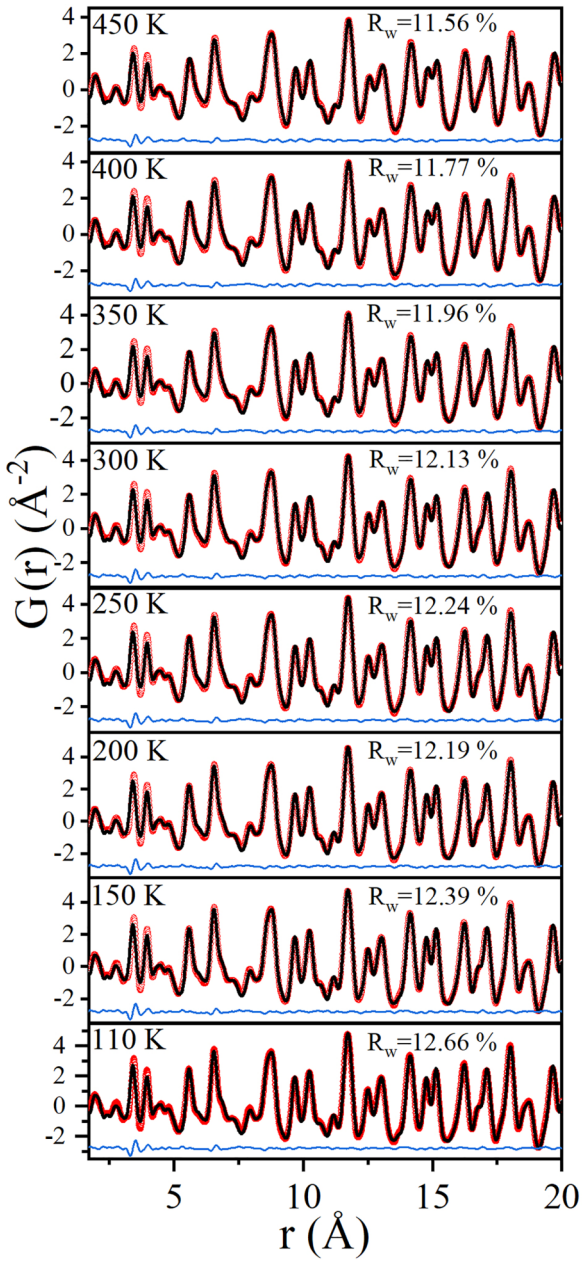


FIG. 8. The experimental (red dots) and calculated (black continuous line) pair distribution functions (PDFs) and their difference (blue line at the bottom) using the tetragonal space group ($P4bm$) in the temperature range 110–450 K obtained by refinement using the PDFGUI program.

(space group: $P4bm$) can be quantified using the amplitude of the ferroelectric phonon mode (Γ_4^-). Figure 9 depicts the evolution of the amplitude of the Γ_4^- (SRO) mode as a function of temperature. The anomalies observed in the temperature-dependent evolution in the amplitude of the ferroelectric phonon mode at critical temperatures, viz. T_B and T_{VF}, corroborate our conclusions inferred from the combined analysis of temperature-dependent dielectric, SXRD, and Raman spectroscopic data. The analysis of experimental PDF reveals that the ferroelectric displacements compatible with antiferrodistorted tetragonal symmetry (space group:

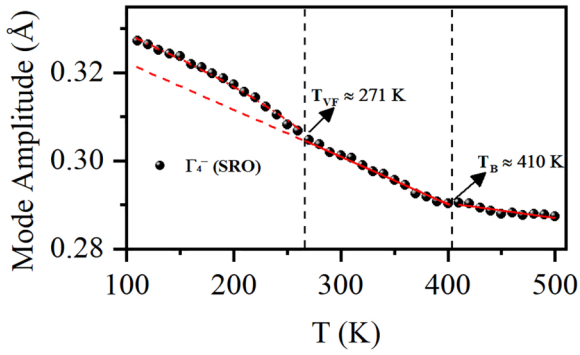


FIG. 9. Temperature dependent evolution of Γ_4^- mode calculated for short-range ordering (SRO) using the information obtained from refinement of PDF patterns.

*P*4*bm*) are present in the temperature range 110 K $\leqslant T \leqslant$ 500 K. Due to a decrease in thermal disorder upon lowering temperatures, the correlated ferroelectric displacements at short ranges form polar nanoregions (characteristic of relaxors) below the Burns temperature ($T_B \approx 410$ K), and eventually transform into a long-range ferroelectrically ordered state below the Vogel-Fulcher freezing temperature ($T_{VF} \approx 270$ K). Moreover, we also notice that the short-range symmetry at high temperatures is the same as the long-range symmetry at low temperatures (i.e., tetragonal with *P*4*bm* space group). This phenomenon is similar to what has been observed earlier for barium titanate and sodium niobate [43,77]. Therefore, relaxor-to-ferroelectric transition in NN-25BCT can be attributed to the enhancement in correlations among PNRs upon decreasing temperatures [18,29,31,36,78].

IV. CONCLUSION

In summary, the dielectric analysis of NN-25BCT reveals relaxor-like behavior with a freezing temperature $T_{VF} \approx$ 270 K. Furthermore, SXRD confirms a long-range relaxor (SG: *P*4/*mbm*) to ferroelectric (SG: *P*4*bm*) phase transition at low temperatures ($T < T_{VF}$). Our experimental work clearly reveals that in-phase octahedral tilting suppresses ferroelectric order on the long-range scale in the perovskite-based systems by exploring the temperature-dependent evolution of the two primary-order parameters, viz. Γ_4^- and M_3^+ obtained using atomic coordinates and lattice parameters extracted from Rietveld analysis. Temperature-dependent Raman spectra reveal the presence of local polar distortions for temperatures above T_{VF}, contrary to the long-range centrosymmetric structure obtained from SXRD. Furthermore, in line with Raman analysis, PDF interpretation provides evidence of local distortions with ferroelectric tetragonal ordering (SG: *P*4*bm*) stable throughout the studied range, i.e., 110 K $\leqslant T \leqslant$ 500 K. Therefore, it is reasonable to believe that the relaxor-to-ferroelectric phase transition originates from the nucleation and growth of a short-range ordered polar tetragonal phase (PNRs with *P*4*bm* symmetry) present in a long-range centrosymmetric matrix (with *P*4/*mbm* space group). This system can be a potential candidate for applications in pyroelectric detectors, electrocaloric devices, multilayered ceramic capacitors (MLCCs), etc.

ACKNOWLEDGMENTS

This research used 28-ID-2 XPD beamlines of the National Synchrotron Light Source II, the National Synchrotron Light Source II, a U.S. Department of Energy (DOE) Office of Science User Facility operated for the DOE Office of Science by Brookhaven National Laboratory under Contract No. DE-SC0012704. S.T. acknowledges financial assistance from the Defence Research and Development Organisation (Grant No. ERIP/ER/202210003/M/01/1812) and DST-SERB, Government of India (Grant No. CRG/2021/006000).

DATA AVAILABILITY

The data that support the findings of this article are not publicly available. The data are available from the authors upon reasonable request.

[1] S.-E. Park and T. R. Shrout, Ultrahigh strain and piezoelectric behavior in relaxor based ferroelectric single crystals, J. Appl. Phys. **82**, 1804 (1997).

[2] V. V. Shvartsman and D. C. Lupascu, Lead-free relaxor ferroelectrics, J. Am. Ceram. Soc. **95**, 1 (2012).

[3] C. W. Ahn, C.-H. Hong, B.-Y. Choi, H.-P. Kim, H.-S. Han, Y. Hwang, W. Jo, K. Wang, J.-F. Li, J.-S. Lee, and I. W. Kim, A brief review on relaxor ferroelectrics and selected issues in lead-free relaxors, J. Korean Phys. Soc. **68**, 1481 (2016)..

[4] A. Bokov and Z.-G. Ye, Recent progress in relaxor ferroelectrics with perovskite structure, J. Mater. Sci. **41**, 31 (2006).

[5] A. Tripathi, A. Pandey, J. A. Alonso, R. Erasmus, M. T. Fernandez-Diaz, and S. Tripathi, Origin of zero thermal expansion in an average cubic structure in Pb-free relaxor ferroelectrics, Appl. Phys. Lett. **125**, 102901 (2024).

[6] M. E. Lines and A. M. Glass, *Principles and Applications of Ferroelectrics and Related Materials* (Oxford University Press, Oxford, 2001).

[7] A. J. Moulson and J. M. Herbert, *Electroceramics: Materials, Properties, Applications* (John Wiley & Sons, New York, 2003).

[8] Y.-H. Bing, A. Bokov, and Z.-G. Ye, Diffuse and sharp ferroelectric phase transitions in relaxors, Curr. Appl. Phys. **11**, S14 (2011).

[9] V. Shvartsman, W. Kleemann, J. Dec, Z. Xu, and S. Lu, Diffuse phase transition in $BaTi_{1-x}Sn_xO_3$ ceramics: An intermediate state between ferroelectric and relaxor behavior, J. Appl. Phys. **99**, 124111 (2006).

[10] T. Maiti, R. Guo, and A. Bhalla, The evolution of relaxor behavior in Ti^{4+} doped $BaZrO_3$ ceramics, J. Appl. Phys. **100**, 114109 (2006).

[11] M. Tyunina and J. Levoska, Coexistence of ferroelectric and relaxor properties in epitaxial films of $Ba_{1-x}Sr_xTiO_3$, Phys. Rev. B **70**, 132105 (2004).

[12] D. N. Dubey, G. Singh, and S. Tripathi, Relaxor ferroelectricity driven by 'A' and 'B' site off-centered displacements in cubic phase with *Pmm* space group, J. Phys. D: Appl. Phys. **54**, 365304 (2021).

[13] H. Kumar and S. Tripathi, Similarities and differences in the ordering at short and long ranges in a $NaNbO_3$ based Pb-free smart system: A key to functional properties, J. Phys. D: Appl. Phys. **57**, 335502 (2024).

[14] L. Cai, J. Toulouse, L. Harriger, R. G. Downing, and L. A. Boatner, Origin of the crossover between a freezing and a structural transition at low concentration in the relaxor ferroelectric $K_{1-x}Li_xTaO_3$, Phys. Rev. B **91**, 134106 (2015).

[15] P. Bonneau, P. Garnier, E. Husson, and A. Morell, Structural study of *Pmn* ceramics by x-ray diffraction between 297 and 1023 K, Mater. Res. Bull. **24**, 201 (1989).

[16] B. Dkhil, J. M. Kiat, G. Calvarin, G. Baldinozzi, S. B. Vakhrushev, and E. Suard, Local and long range polar order in the relaxor-ferroelectric compounds $PbMg_{1/3}Nb_{2/3}O_3$ and $PbMg_{0.3}Nb_{0.6}Ti_{0.1}O_3$, Phys. Rev. B **65**, 024104 (2001).

[17] Z.-G. Ye, Y. Bing, J. Gao, A. Bokov, P. Stephens, B. Noheda, and G. Shirane, Development of ferroelectric order in relaxor $(1-x)Pb(Mg_{1/3}Nb_{2/3})O_3 - xPbTiO_3$ ($0 <\sim x <\sim 0.15$), Phys. Rev. B **67**, 104104 (2003).

[18] A. Tripathi, S. Ghose, R. Erasmus, and S. Tripathi, Evidence of distinct nonpolar/polar ordering at long/short ranges in relaxor ferroelectrics, Phys. Rev. B **111**, 024104 (2025).

[19] S. Kojima, R. Ohta, T. Ariizumi, and J. Zushi, Dynamic polar nanoregions and broken local symmetry in relaxor ferroelectrics probed by inelastic light scattering, *Journal of Physics: Conference Series*, Vol. 428 (IOP Publishing, 2013), p. 012027.

[20] G. Burns and F. Dacol, Glassy polarization behavior in ferroelectric compounds $Pb(Mg_{1/3}Nb_{2/3})O_3$ and $Pb(Zn_{1/3}Nb_{2/3})O_3$, Solid State Commun. **48**, 853 (1983).

[21] D. Viehland, S. J. Jang, L. E. Cross, and M. Wuttig, Deviation from Curie-Weiss behavior in relaxor ferroelectrics, Phys. Rev. B **46**, 8003 (1992).

[22] D. La-Orauttapong, J. Toulouse, J. L. Robertson, and Z.-G. Ye, Diffuse neutron scattering study of a disordered complex perovskite $Pb(Zn_{1/3}Nb_{2/3})O_3$ crystal, Phys. Rev. B **64**, 212101 (2001).

[23] D. La-Orauttapong, J. Toulouse, Z.-G. Ye, W. Chen, R. Erwin, and J. L. Robertson, Neutron scattering study of the relaxor ferroelectric $(1-x)Pb\,(Zn_{1/3}Nb_{2/3})O_3 - xPbTiO_3$, Phys. Rev. B **67**, 134110 (2003).

[24] M. Roth, E. Mojaev, E. Dul'kin, P. Gemeiner, and B. Dkhil, Phase transition at a nanometer scale detected by acoustic emission within the cubic phase $Pb(Zn_{1/3}Nb_{2/3})O_3 - xPbTiO_3$ relaxor ferroelectrics, Phys. Rev. Lett. **98**, 265701 (2007).

[25] D. Viehland, S. Jang, L. Eric Cross, and M. Wuttig, The dielectric relaxation of lead magnesium niobate relaxor ferroelectrics, Philos. Mag. B **64**, 335 (1991).

[26] D. Viehland, J. F. Li, S. J. Jang, L. E. Cross, and M. Wuttig, Dipolar-glass model for lead magnesium niobate, Phys. Rev. B **43**, 8316 (1991).

[27] J. Zhao, A. Glazounov, Q. Zhang, and B. Toby, Neutron diffraction study of electrostrictive coefficients of prototype cubic phase of relaxor ferroelectric $PbMg_{1/3}Nb_{2/3}O_3$, Appl. Phys. Lett. **72**, 1048 (1998).

[28] F. Chu, I. Reaney, and N. Setter, Investigation of relaxors that transform spontaneously into ferroelectrics, Ferroelectrics **151**, 343 (1994).

[29] X. Dai, Z. Xu, and D. Viehland, The spontaneous relaxor to normal ferroelectric transformation in La-modified lead zirconate titanate, Philos. Mag. B **70**, 33 (1994).

[30] V. R. Mastelaro, Y. P. Mascarenhas, P. Neves, M. Mir, A. C. Doriguetto, A. Michalowicz, J. Moscovici, M. Lente, and J. A. Eiras, Spontaneous long and short-range ferroelectric ordering in $Pb_{0.55}La_{0.3}TiO_3$ ceramics, J. Appl. Phys. **107**, 114103 (2010).

[31] X. Dai and D. Viehland, Tetragonal-structured PLZT relaxor ferroelectrics, Ferroelectrics **158**, 375 (1994).

[32] H. Arndt, F. Sauerbier, G. Schmidt, and L. Shebanov, Field-induced phase transition in $Pb(Mg_{1/3}Nb_{2/3})O_3$ single crystals, Ferroelectrics **79**, 145 (1988).

[33] X. Zhao, W. Qu, X. Tan, A. A. Bokov, and Z.-G. Ye, Electric field-induced phase transitions in (111)-,(110)-, and (100)-oriented $Pb(Mg_{1/3}Nb_{2/3})O_3$ single crystals, Phys. Rev. B **75**, 104106 (2007).

[34] P. Juhás, T. Davis, C. L. Farrow, and S. J. Billinge, PDFgetX3: a rapid and highly automatable program for processing powder diffraction data into total scattering pair distribution functions, J. Appl. Crystallogr. **46**, 560 (2013).

[35] C. Farrow, P. Juhas, J. Liu, D. Bryndin, E. Božin, J. Bloch, T. Proffen, and S. Billinge, PDFfit2 and PDFgui: computer programs for studying nanostructure in crystals, J. Phys.: Condens. Matter **19**, 335219 (2007).

[36] D. Viehland, S. Jang, L. E. Cross, and M. Wuttig, Freezing of the polarization fluctuations in lead magnesium niobate relaxors, J. Appl. Phys. **68**, 2916 (1990).

[37] X. Long and Z.-G. Ye, Relaxor behavior in the solid solution between dielectric $Ba(Mg_{1/3}Nb_{2/3})O_3$ and ferroelectric $PbTiO_3$, Appl. Phys. Lett. **90**, 112905 (2007).

[38] V. Shvartsman, J. Zhai, and W. Kleemann, The dielectric relaxation in solid solutions $BaTi_{1-x}Zr_xO_3$, Ferroelectrics **379**, 77 (2009).

[39] F. Chu, I. Reaney, and N. Setter, Spontaneous (zero-field) relaxor to ferroelectric-phase transition in disordered $Pb(Sc_{1/2}Nb_{1/2})O_3$, J. Appl. Phys. **77**, 1671 (1995).

[40] L. Wang, H. Qi, B. Gao, Y. Liu, H. Liu, and J. Chen, Large piezoelectricity in $NaNbO_3$-based lead-free ceramics via tuning oxygen octahedral tilt, Mater. Horiz. **9**, 1002 (2022).

[41] A. M. Glazer, The classification of tilted octahedra in perovskites, Acta Cryst. B **28**, 3384 (1972).

[42] A. Glazer, Simple ways of determining perovskite structures, Acta Cryst. A **31**, 756 (1975).

[43] L. Jiang, D. C. Mitchell, W. Dmowski, and T. Egami, Local structure of $NaNbO_3$: A neutron scattering study, Phys. Rev. B **88**, 014105 (2013).

[44] L. Wang, S. Sun, H. Luo, Y. Ren, H. Liu, X. Xing, and J. Chen, Boosted piezoelectricity with excellent thermal stability in tetragonal $NaNbO_3$-based ceramics, J. Mater. Chem. A **9**, 2367 (2021).

[45] J. Rodríguez-Carvajal, Recent advances in magnetic structure determination by neutron powder diffraction, Phys. B (Amsterdam, Neth.) **192**, 55 (1993).

[46] M. Jauhari, S. K. Mishra, R. Mittal, P. U. Sastry, and S. L. Chaplot, Effect of chemical pressure on competition and cooperation between polar and antiferrodistortive distortions in sodium niobate, Phys. Rev. Mater. **1**, 074411 (2017).

[47] See Supplemental Material at http://link.aps.org/supplemental/10.1103/szgf-l5rt for details on Rietveld fits of diffraction patterns, structural models used in Rietveld refinements, and deconvoluted Raman spectra..

[48] D. Orobengoa, C. Capillas, M. I. Aroyo, and J. M. Perez-Mato, AMPLIMODES: symmetry-mode analysis on the Bilbao Crystallographic Server, J. Appl. Cryst. **42**, 820 (2009).

[49] J. Perez-Mato, D. Orobengoa, and M. Aroyo, Mode crystallography of distorted structures, Acta Cryst. A **66**, 558 (2010).

[50] W. Zhong and D. Vanderbilt, Competing structural instabilities in cubic perovskites, Phys. Rev. Lett. **74**, 2587 (1995).

[51] N. Sai and D. Vanderbilt, First-principles study of ferroelectric and antiferrodistortive instabilities in tetragonal $SrTiO_3$, Phys. Rev. B **62**, 13942 (2000).

[52] U. Aschauer and N. A. Spaldin, Competition and cooperation between antiferrodistortive and ferroelectric instabilities in the model perovskite $SrTiO_3$, J. Phys.: Condens. Matter **26**, 122203 (2014).

[53] N. A. Benedek and C. J. Fennie, Why are there so few perovskite ferroelectrics? J. Phys. Chem. C **117**, 13339 (2013).

[54] H. Wieder, Electrical behavior of barium titanate single crystals at low temperatures, Phys. Rev. **99**, 1161 (1955).

[55] C.-J. Eklund, C. J. Fennie, and K. M. Rabe, Strain-induced ferroelectricity in orthorhombic $CaTiO_3$ from first principles, Phys. Rev. B **79**, 220101(R) (2009).

[56] S. Bhattacharjee, E. Bousquet, and P. Ghosez, Engineering multiferroism in $CaMnO_3$, Phys. Rev. Lett. **102**, 117602 (2009).

[57] A. J. Hatt and N. A. Spaldin, Structural phases of strained $LaAlO_3$ driven by octahedral tilt instabilities, Phys. Rev. B **82**, 195402 (2010).

[58] S. Gupta, R. Katiyar, R. Guo, and A. Bhalla, Study of structural phase transitions in solid-solution $(1-x)$PZN–xPT relaxor ferroelectric using Raman scattering, J. Raman Spectrosc. **31**, 921 (2000).

[59] P. Dobal, R. Katiyar, and C.-S. Tu, Study of ordered nanoregions in $Pb(Zn_{1/3}Nb_{2/3})_{0.915}Ti_{0.085}O_3$ single crystal using Raman spectroscopy, J. Raman Spectrosc. **34**, 152 (2003).

[60] J. Kreisel and P. Bouvier, High-pressure Raman spectroscopy of nano-structured ABO_3 perovskites: a case study of relaxor ferroelectrics, J. Raman Spectrosc. **34**, 524 (2003).

[61] O. Svitelskiy, J. Toulouse, G. Yong, and Z.-G. Ye, Polarized Raman study of the phonon dynamics in $Pb(Mg_{1/3}Nb_{2/3})O_3$ crystal, Phys. Rev. B **68**, 104107 (2003).

[62] P. Krishna, S. Mishra, A. Shinde, S. Kesari, and R. Rao, Raman spectroscopy of lithium modified sodium niobate at elevated temperature, Ferroelectrics **510**, 34 (2017).

[63] G. de la Flor, T. Malcherek, S. Gorfman, and B. Mihailova, Structural transformations in $(1-x)Na_{0.5}Bi_{0.5}TiO_3 - xBaTiO_3$ single crystals studied by Raman spectroscopy, Phys. Rev. B **96**, 214102 (2017).

[64] Y. Shiratori, A. Magrez, J. Dornseiffer, F.-H. Haegel, C. Pithan, and R. Waser, Polymorphism in micro-, submicro-, and nanocrystalline $NaNbO_3$, J. Phys. Chem. B **109**, 20122 (2005).

[65] K.-i. Kakimoto, K. Akao, Y. Guo, and H. Ohsato, Raman scattering study of piezoelectric $(Na_{0.5}K_{0.5})$ NbO_3-$LiNbO_3$ ceramics, Jpn. J. Appl. Phys. **44**, 7064 (2005).

[66] R. Zuo, H. Qi, J. Fu, J.-F. Li, and L. Li, Multiscale identification of local tetragonal distortion in $NaNbO_3$-$BaTiO_3$ weak relaxor ferroelectrics by Raman, synchrotron x-ray diffraction, and absorption spectra, Appl. Phys. Lett. **111**, 132901 (2017).

[67] K. A. Schönau, L. A. Schmitt, M. Knapp, H. Fuess, R.-A. Eichel, H. Kungl, and M. J. Hoffmann, Nanodomain structure of $Pb[Zr_{1-x}\ Ti_x]O_3$ at its morphotropic phase boundary: Investigations from local to average structure, Phys. Rev. B **75**, 184117 (2007).

[68] I. Grinberg, V. R. Cooper, and A. M. Rappe, Relationship between local structure and phase transitions of a disordered solid solution, Nature (London) **419**, 909 (2002).

[69] T. Egami, W. Dmowski, M. Akbas, and P. Davies, Local structure and polarization in Pb containing ferroelectric oxides, *AIP Conference Proceedings* (American Institute of Physics, 1998), Vol. 436, pp. 1–10.

[70] W. Dmowski, M. Akbas, P. Davies, and T. Egami, Local structure of Pb $(Sc_{1/2},Ta_{1/2})O_3$ and related compounds, J. Phys. Chem. Solids **61**, 229 (2000).

[71] T. Egami, Local structure of ferroelectric materials, Annu. Rev. Mater. Res. **37**, 297 (2007).

[72] S. J. Billinge, The atomic pair distribution function: past and present, Z. Krist.-Cryst. Mater. **219**, 117 (2004).

[73] S. J. Billinge and M. G. Kanatzidis, Beyond crystallography: the study of disorder, nanocrystallinity and crystallographically challenged materials with pair distribution functions, Chem. Commun. 749 (2004).

[74] D. Fu, M. Itoh, and S.-Y. Koshihara, Invariant lattice strain and polarization in $BaTiO_3$-$CaTiO_3$ ferroelectric alloys, J. Phys.: Condens. Matter **22**, 052204 (2010).

[75] L. Kozielski, A. Wilk, M. M. Bućko, and J. Banys, A large piezoelectric strain recorded in BCT ceramics obtained by a modified Pechini method, Materials **13**, 1620 (2020).

[76] H. Kumar, S. Ghose, R. Erasmus, and S. Tripathi, Multiscale structural analysis of polymorphic phase boundaries in doped antiferroelectric sodium niobate, Phys. Rev. B **111**, 054108 (2025).

[77] M. S. Senn, D. A. Keen, T. C. A. Lucas, J. A. Hriljac, and A. L. Goodwin, Emergence of long-range order in $BaTiO_3$ from local symmetry-breaking distortions, Phys. Rev. Lett. **116**, 207602 (2016).

[78] L. Mitoseriu, A. Stancu, C. Fedor, and P. M. Vilarinho, Analysis of the composition-induced transition from relaxor to ferroelectric state in $PbFe_{2/3}W_{1/3}O_3$-$PbTiO_3$ solid solutions, J. Appl. Phys. **94**, 1918 (2003).